bioRxiv preprint doi: https://doi.org/10.1101/314484; this version posted May 4, 2018. The copyright holder for this preprint (which was not certified by peer review) is the author/funder. All rights reserved. No reuse allowed without permission.

1 # Polarity sorting drives remodeling of
2 # actin-myosin networks

3 Viktoria Wollrab[1], Julio M. Belmonte[2], Maria Leptin[2], François Nédeléc[2,*], Gijsje H. Koenderink[1,*]
4

5 [1]AMOLF, Science Park 104, 1098 XG Amsterdam

6 [2]EMBL, Cell Biology and Developmental Biology Unit and Director's Research Unit, Meyerhofstraße 1,
7 Heidelberg

8 [*]Corresponding author: g.koenderink@amolf.nl (G.H.K.), nedelec@embl.de (F.N.)

9 ## Abstract
10 Cytoskeletal networks of actin filaments and myosin motors drive many dynamic cell processes. A key
11 characteristic of these networks is their contractility. Despite intense experimental and theoretical
12 efforts, it is not clear what mechanism favors network contraction over expansion. Recent work points to
13 a dominant role for the nonlinear mechanical response of actin filaments, which can withstand
14 stretching but buckle upon compression. Here we present an alternative mechanism. We study how
15 interactions between actin and myosin-2 at the single filament level translate into contraction at the
16 network scale by performing time-lapse imaging on reconstituted quasi-2D-networks mimicking the cell
17 cortex. We observe myosin end-dwelling after it runs processively along actin filaments. This leads to
18 transport and clustering of actin filament ends and the formation of transiently stable bipolar structures.
19 Further we show that myosin-driven polarity sorting leads to polar actin aster formation, which act as
20 contractile nodes that drive contraction in crosslinked networks. Computer simulations comparing the
21 roles of the end-dwelling mechanism and a buckling-dependent mechanism show that the relative
22 contribution of end-dwelling contraction increases as the network mesh-size decreases.

23

24 ## Introduction
25 Cells have the remarkable ability to actively deform themselves to drive vital processes such as cell
26 division, cell migration and multicellular tissue dynamics. The main determinant of cell shape is the actin
27 cytoskeleton, which actively deforms the plasma membrane by generating pushing and pulling forces
28 (Blanchoin et al., 2014). This activity relies on the structural polarity of actin filaments, which have
29 structurally distinct ends denoted as the *minus* and the *plus end* (also referred to as the pointed and the
30 barbed end). Hydrolysis of adenosine triphosphate (ATP) bound to actin monomers that add onto the
31 plus end of growing filaments provides chemical energy, which allows actin filaments to exert
32 polymerization forces at their plus ends. Myosin-2 motors take advantage of the structural polarity of F-

bioRxiv preprint doi: https://doi.org/10.1101/314484; this version posted May 4, 2018. The copyright holder for this preprint (which was not certified by peer review) is the author/funder. All rights reserved. No reuse allowed without permission.

33 actin to move in a directional manner toward the plus end, again using energy released from ATP
34 hydrolysis. The motors work together in teams known as bipolar filaments, with motor heads on the two
35 ends and the tails packed in the center. This bipolarity allows myosin filaments to slide anti-parallel actin
36 filaments in opposing directions.

37 Together with accessory crosslinking proteins, actin and myosin-2 form different contractile assemblies
38 in the cell (Murrell et al., 2015). Right underneath the plasma membrane, they form a thin and dense
39 polymer mesh known as the cortex. A key function of the cortex is its contractility, which can drive global
40 cell rounding as cells enter mitosis, local membrane constriction during cell division, and global tissue
41 deformation in developing embryos (Salbreux et al., 2012). In the cytoplasm, actin and myosin form
42 bundled contractile structures known as stress fibers in adherent cells and 3D-meshworks in large
43 oocytes and early embryo cells (Field and Lénárt, 2011; Naumanen et al., 2008). Finally, during
44 cytokinesis, actin and myosin form a contractile structure known as the cytokinetic ring, which constricts
45 the membrane (Wollrab et al., 2016).

46 Despite detailed knowledge of the molecular composition of the actin-myosin 'contractome' (Biro et al.,
47 2013; Zaidel-Bar et al., 2015), the molecular mechanism for the contractile activity of the actin-myosin
48 cytoskeleton is unclear since the actomyosin bundles and meshworks in nonmuscle cells are disordered
49 in terms of the filament orientations and polarities. This is completely unlike muscle sarcomeres, where
50 the actin and myosin are arranged in repeating arrays with myosin bipolar filaments localized in-between
51 antiparallel actin filaments having their minus ends inwards and their plus ends outwards. In this case,
52 the localization of the myosin clusters in the vicinity of F-actin minus ends and the anchoring of the actin
53 filament minus ends at the Z-discs convert the sliding activity of the motors into pure contraction (Gautel
54 and Djinovic-Carugo, 2016). By contrast, motor-mediated sliding of rigid filaments in random networks is
55 in principle equally likely to result in contraction or expansion (Belmonte et al., 2017; Mendes Pinto et
56 al., 2012). Experimentally, both contraction and expansion have indeed been demonstrated in
57 reconstituted networks of microtubules and motors (Foster et al., 2015; Sanchez et al., 2012; Torisawa et
58 al., 2016) and in cells (Lu et al., 2013). In contrast, actomyosin assemblies in cells always contract, and
59 reconstituted networks of actin filaments and myosin motors are also nearly always contractile (Stam et
60 al., 2017).

61 It has been a long-standing question why actin-myosin networks are biased towards contraction and
62 different microscopic mechanisms have been proposed (Alvarado et al., 2017). The currently most
63 favored mechanism is based on the nonlinear elastic properties of actin filaments. Actin filaments are
64 semiflexible polymers with a persistence length of around 10 µm (Kang et al., 2012). As a consequence,
65 they resist stretching but readily buckle upon compression forces induced by molecular motors.
66 Theoretical models of active networks predict that buckling will cause contraction in both bundles and
67 meshworks, independent of filament polarity (Lenz et al., 2012; Ronceray et al., 2016). Effectively,
68 myosin bipolar filaments interacting with crosslinked actin networks act as contractile force dipoles
69 (Mackintosh and Levine, 2008). This buckling scenario is supported by direct experimental observations
70 of filament buckling and telescopic contraction in reconstituted actin-myosin bundles and random
71 networks (Linsmeier et al., 2016; Murrell and Gardel, 2012).

bioRxiv preprint doi: https://doi.org/10.1101/314484; this version posted May 4, 2018. The copyright holder for this preprint (which was not certified by peer review) is the author/funder. All rights reserved. No reuse allowed without permission.

72 Yet, analytical and computational models predict that preferential contraction can also occur in the
73 absence of filament buckling. The basic idea is that if motors processively walk along cytoskeletal
74 filaments towards one end (the plus end in case of myosin-2) and dwell before they detach, they will
75 cause polarity sorting of the filaments and eventually contraction of both bundles and networks (Kruse
76 and Jülicher, 2000; Zumdieck et al., 2007). In networks, a clear signature of polarity sorting is the
77 formation of radial arrays of filaments known as asters, where the filament ends point inwards and
78 motors accumulate in the center. In case of microtubule systems, several motors have indeed been
79 shown to exhibit end-dwelling behavior (Akhmanova and Hoogenraad, 2005) and cause the formation of
80 polar asters (Foster et al., 2015; Surrey et al., 2001; Torisawa et al., 2016). While this phenomenon is
81 now well accepted for microtubules (Tan et al., 2018), it is not known whether it can also operate for
82 actin. In case of myosin-2, there are observations of processive motion along actin filaments in motility
83 assays and in dense actin-myosin networks (Sellers and Kachar, 1990; Soares e Silva et al., 2011; Vogel et
84 al., 2013), but it is unknown whether myosin motors dwell at actin filament plus ends. There are
85 intriguing observations of polar aster formation indicative of polarity sorting in cells (Verkhovsky et al.,
86 1997) and in reconstituted assays (Backouche et al., 2006; Köster et al., 2016; Soares e Silva et al., 2011),
87 but there is to our knowledge no direct evidence of myosin-mediated polarity sorting. Studies of
88 contraction in actin-myosin networks have typically been performed at high protein densities, precluding
89 direct observation of the interactions between actin and myosin at the single filament level.

90 Here we study how interactions between actin and myosin-2 at the single filament level translate into
91 contractile activity at the network scale by performing time-lapse fluorescence imaging on reconstituted
92 quasi 2D-networks of actin filaments and myosin motors. This 2D geometry mimics the quasi-2D random
93 organization of the actin cortex and furthermore facilitates high resolution imaging of actin-myosin
94 interactions at the single-filament level. Since actin-myosin remodeling is rather fast, we develop an
95 open chamber assay that allows us to capture the initial steps of myosin-mediated remodeling
96 immediately following the addition of components that trigger contractile activity. We show that
97 myosin-2 bipolar filaments remodel initially random actin meshworks into polar asters. Experiments at
98 low filament densities reveal that single myosin filaments processively walk towards actin filament plus
99 ends, where they dwell. This end-dwelling behavior allows myosin filaments to transport actin filament
100 ends together to form asters. By observing actomyosin remodeling over a range of time and length
101 scales, we show that the polarity sorting at the single filament level drives aster formation and
102 subsequent local or global network contraction, depending on the network connectivity. We use
103 computer simulations to estimate the importance that polarity sorting and buckling may have for
104 contraction *in vivo*, where the filaments are shorter and the network is denser than in our experiments *in*
105 *vitro*.

106
Results

107 To resolve the mechanism by which myosin drives remodeling of actin networks, we reconstitute two-
108 dimensional networks of skeletal muscle actin and myosin labeled in different fluorescent colors on
109 nonadherent glass surfaces and observe remodeling by total internal reflection fluorescence (TIRF)
110 microscopy. Myosin-driven remodeling is a fast process whereby initial changes to the actin network

bioRxiv preprint doi: https://doi.org/10.1101/314484; this version posted May 4, 2018. The copyright holder for this preprint (which was not certified by peer review) is the author/funder. All rights reserved. No reuse allowed without permission.

111 happen on second time scales. In traditional flow cell setups these events would be difficult to capture.
112 Therefore we use an open chamber setup, which allows us to trigger remodeling by adding myosin or
113 ATP during the time-lapse acquisition (Fig. 1a, Video 1). When we add myosin to a pre-polymerized,
114 random actin network, we observe that myosin starts to remodel actin as soon as it reaches the imaging
115 surface (Fig. 1b). Within 40 seconds, this remodeling leads to the formation of actin asters with dense
116 myosin foci at their center. Time-lapse imaging of the trajectories of myosins shows that they move
117 directionally inward toward the center of the aster, implying that the asters are polar with actin plus
118 ends oriented inwards (Fig. 1c and 1d). We conclude that myosin can remodel an initially random
119 network of actin filaments within seconds into an organized network containing polar structures.

120 To understand how the motors achieve polarity sorting, we used more diluted conditions where we can
121 observe interactions of single myosin bipolar filaments with single actin filaments. We trigger myosin
122 activity by adding ATP to a network of pre-polymerized actin and myosin. Prior to ATP addition, the actin
123 filaments are densely decorated with myosin (left-most panel in Fig. 2a, Video 2), which is known to bind
124 strongly in the absence of ATP. Under this condition, the actin filaments form bundles, likely due to the
125 combination of the myosins acting as crosslinkers and the presence of a crowding agent. Upon ATP
126 addition, most myosin filaments release, consistent with the low duty ratio of myosin-2 (Harris and
127 Warshaw, 1993). The actin bundle disassembles in single filaments, likely due to the absence of
128 crosslinking myosin. The remaining myosin filaments unidirectionally run along the actin filaments with a
129 typical mean speed of 2 µm/s (Fig. 2b). We do not observe myosin detachment from the actin filaments
130 unless the myosin filament encounters another actin filament, whereafter it switches track and runs
131 along the new actin filament (after 28 seconds in Fig. 2a). As myosin reaches the end of the actin
132 filament, it dwells on it. This can lead to an accumulation of myosin if several myosins run along the
133 same actin filament (Fig. 2c, Video 3).

134 Myosin end-dwelling on single actin filament ends is a common event (Fig. 3a). This configuration is
135 stable for at least several minutes. To determine a lower limit for the end dwelling time, we observed
136 myosin end-dwelling for at least 4 minutes. In only 6% of the cases (n = 36), myosin detached during this
137 time. From this we estimate a characteristic dwell-time of 64 min, assuming a Poisson process (see SI).
138 We also find end-dwelling events that last over 15 min. Interestingly, myosin and actin ends seem not to
139 overlap completely, which becomes clearer when we plot line profiles of the myosin and actin intensities
140 (Fig. 3b). By analyzing these line profiles, we infer the length of the myosin filaments and overlap of the
141 myosin and actin filament. We determine the average myosin length as 0.8 µm (Fig. 3c), in agreement
142 with transmission electron microscopy data (Suppl. Fig. 1). The average overlap of the myosin and actin
143 filaments is only 50% (Fig. 3c). This suggests that myosin filaments exhibit end-dwelling because of their
144 "bipolarity" as sketched in Fig. 3d, consistent with prior reports of an interaction of F-actin with the
145 trailing end of the bipolar myosin filament (Sellers and Kachar, 1990; Yamada and Wakabayashi, 1993).

146 We then wondered whether the processive motion and end-dwelling behavior of myosin can account for
147 the formation of actin asters via polarity sorting, given that theoretical models and simulations predict
148 that these are necessary and sufficient ingredients (Surrey et al., 2001). Therefore we increased the actin
149 filament concentration so that filaments overlap. We again observe that end-dwelling is a common event
150 (Fig. 4a, yellow circles). Furthermore we see many examples of myosin connecting filament ends to form

bioRxiv preprint doi: https://doi.org/10.1101/314484; this version posted May 4, 2018. The copyright holder for this preprint (which was not certified by peer review) is the author/funder. All rights reserved. No reuse allowed without permission.

151 incipient asters (Fig. 4a, cyan circles). To understand the formation of these structures, we turned to live
152 imaging. We see that myosin that is already bound to the end of one actin filament can still processively
153 run along another actin filament (Fig. 4b, Video 4). As it arrives at the other filament's end, it dwells also
154 there and thereby holds the filament ends together. These bipolar structures can grow further and catch
155 additional actin filaments (Suppl. Fig. 2). This observation shows that myosin end dwelling together with
156 its processivity can be a mechanism to transport filament ends toward each other, as sketched in Fig. 4c.
157 At concentrations of filaments and myosin used in this assay, the incipient aster configurations are not
158 stable. Myosin can detach from one of the filaments while staying attached to the other (Fig. 4b, last
159 time point). We used higher actin filament concentrations to test whether this mechanism is also active
160 in dense networks (Fig. 4d, Video 5). We see the same mechanism: As myosin runs along one filament
161 (cyan), it encounters a second filament (yellow). Subsequently it moves on both filaments and stops
162 when it arrives at the two filament ends. This configuration is stable for a few minutes until myosin
163 switches to another filament and starts to move on that one (Fig. 4d, last time point). Taking all this
164 together, we conclude that myosin end dwelling together with processive motion can transport filament
165 ends together, connect them in transiently stable complexes, and thereby induce polarity sorting.

166 We next tested whether polar structures are also present at actin densities studied in prior
167 reconstitution studies of contractility in actin-myosin networks (Murrell and Gardel, 2014, 2012; Vogel et
168 al., 2013). We observed that asters still form and are rather stable (Fig. 5a), although we occasionally
169 observe events where the aster splits (Fig. 5c, Video 6). The splitting of asters could be linked to the
170 ability of the myosins to detach from filament ends when they get the option to switch to another actin
171 filament track, as we observed at low filament densities.

172 Since asters are polar, they should in principle be able to merge due to the action of myosin motors. We
173 indeed observe that neighboring asters interact. An example is shown in Fig. 5b: The two asters move
174 toward one another but also away from each other along the same line. This one dimensional back and
175 forth movement is clearly visible in the kymograph representation. Eventually the asters in this example
176 merge. Interestingly we also observe exchange of myosin between asters (Fig. 5d).

177 We hypothesized that in order to increase aster interaction, we need to increase the network
178 connectivity by adding a crosslinking agent. This hypothesis is based on evidence from *in vitro* studies,
179 cells, and theoretical models that crosslinkers increase the range of force transmission by creating a
180 percolated network (Alvarado et al., 2013; Bendix et al., 2008; Ennomani et al., 2016; Koenderink et al.,
181 2009; Köhler et al., 2011; Laporte et al., 2012; Ojkic et al., 2011). Indeed, when we add the crosslinking
182 protein α-actinin-1 (Ciobanasu et al., 2014), we observe that the asters are much larger, persistently
183 move towards each other over distances of tens of µm, and invariably merge (Fig. 5e-g, Video 7). Long-
184 range force transmission is mediated by α-actinin-rich actin bundles, which connect the asters (Suppl.
185 Fig. 3). In addition to growing by merging, asters can also grow by a radial inward flow of actin filaments
186 and myosin along the aster arms (Suppl. Fig. 4, Video 8). We conclude that crosslinkers favor contraction
187 not only by providing elastic connections but also by allowing formation of stable F-actin bundle tracks
188 that promote inward transport of myosin to form stable asters. Moreover, they form stable connections
189 of mixed polarity between asters, stimulating aster merging (sketched in Fig. 5h). However, passive
190 crosslinkers and motors acting together constitute the elementary configuration of the buckling

bioRxiv preprint doi: https://doi.org/10.1101/314484; this version posted May 4, 2018. The copyright holder for this preprint (which was not certified by peer review) is the author/funder. All rights reserved. No reuse allowed without permission.

191 mechanisms (Belmonte et al., 2017). Thus, in addition to helping the sorting mechanism, adding α-
192 actinin is likely to promote the buckling mechanism as well.

193 We asked how this polarity sorting influences network contraction on large scales. As reported
194 previously (Alvarado et al., 2013; Belmonte et al., 2017; Bendix et al., 2008), the balance between
195 crosslinking and motor activity is a key parameter controlling the contractile behavior of actin-myosin
196 networks. We fix the α-actinin concentration such that its molar ratio with actin is R_C = 1:50, which is
197 well above the percolation threshold for 2D networks (Alvarado et al., 2017). To explore different
198 regimes, we vary the myosin concentration. We confine actin-myosin networks containing 0.1 mM ATP
199 in large ~2mm by 22mm chambers with non-adhesive walls and image the entire network over time
200 using a low-NA (10x) objective, starting when contractility is triggered by mixing actin and myosin in the
201 presence of ATP. Starting with a high myosin-to-actin ratio, R_M = 0.05, we find network contraction only
202 on short length scales (Fig. 6a, magenta, Video 9). When we image the dense actin-myosin clusters at
203 higher magnification, we find that they are comprised of actin asters with myosin foci at their core (Fig.
204 6b, magenta). As we decrease the motor-to-actin ratio R_M to 0.01, we still find actin asters but
205 embedded in a fully percolated network as evidenced by a global network contraction (Fig. 6a). At higher
206 magnification, we observe that the network is again made of asters (Fig. 6b). Decreasing R_M even further
207 to 0.005 leads to stalled networks that are unable to contract (Fig. 6a, blue). Also here we observe asters
208 at higher magnification (Fig. 6b). We suggest that two effects play a role in the contraction process. On
209 the one hand, myosin accumulates in the center of the aster and is therefore depleted in the other areas,
210 which do not experience major remodeling anymore. On the other hand aster arms have to overlap with
211 neighboring aster centers to contract. These connections are more stable for lower myosin
212 concentrations. As schematically depicted in Fig. 6c, our experimental results suggest that aster
213 formation contributes to both local and global contraction.

214 While these large networks contract in the presence of both end-dwelling myosin-2 and α-actinin
215 crosslinkers, it is not clear from the experiments if the observed contraction of the networks is due to a
216 polarity-sorting mechanism alone or if the buckling mechanism or other effects are also working in
217 parallel (Belmonte et al., 2017; Lenz et al., 2012; Ronceray et al., 2015). We can also not judge from our
218 *in vitro* experiments to what extent this novel mode of contraction of actomyosin networks plays a role
219 in physiological conditions, where both the filaments and mesh sizes are much smaller (Bovellan et al.,
220 2014; Eghiaian et al., 2015; Fritzsche et al., 2016; Fujiwara et al., 2016). We thus turned to computer
221 simulations of actin networks with the software Cytosim (Nédélec and Foethke, 2007), which allows us to
222 approach *in vitro* and cortex-like conditions and analyze the relative contributions of end-dwelling and
223 buckling mechanisms in networks of higher density.

224 We model individual filaments, myosin minifilament and α-actinin crosslinker explicitly, as described in
225 the Methods section. While Cytosim has been used in the past to study both the buckling mechanism
226 (Belmonte et al., 2017) and the polarity mechanism (Surrey et al., 2001) independently from each other,
227 the current assumptions allow both mechanisms to operate in parallel here. Polarity sorting depends on
228 the ability of the motors to end-dwell but does not require crosslinkers. Buckling-mediated contraction
229 requires crosslinkers but operates even if the motors do not end-dwell. With simulations, we can thus
230 enable or disable end-dwelling and add or remove crosslinkers to assess the influence of the two

bioRxiv preprint doi: https://doi.org/10.1101/314484; this version posted May 4, 2018. The copyright holder for this preprint (which was not certified by peer review) is the author/funder. All rights reserved. No reuse allowed without permission.

231 mechanisms. We first modeled contraction of actin networks with myosin minifilaments but no
232 crosslinkers, with myosin dwelling at filament ends. The end-dwelling property of myosin heads leads to
233 the formation of asters (Fig. 7a, Video 10), with all the plus ends facing inwards (Fig. 7a, last panel),
234 resembling the asters observed *in vitro* (Fig. 1). If we let the motor heads detach immediately upon
235 reaching the end of actin filaments, the network fails to contract (Fig. 7b, Video 11). These results
236 confirm the role of end-dwelling for the contractility observed in the *in vitro* networks.

237 We next added α-actinin crosslinkers and systematically varied the concentration of myosin and
238 α–actinin (Fig. 7c). We can observe all three network behaviors seen in the *in vitro* experiments: slow or
239 stalled networks, for high concentrations of α-actinin and low concentrations of myosin; globally
240 contracted networks for high myosin concentrations; and locally contracted asters for low myosin and α-
241 actinin concentrations. To assess the contribution of polarity-sorting to the contraction of the networks,
242 we repeated the simulations with the end-dwelling turned off (Fig. 7d). In this scenario most of the
243 networks fail to contract, indicating an important role of polarity sorting in the contraction of actin
244 networks. The region of the phase diagram least affected by the absence of end-dwelling is characterized
245 by high concentrations of crosslinkers, a condition that is crucial in the filament buckling mechanism, as
246 shown previously by theory and simulations (Belmonte et al., 2017; Lenz et al., 2012) and experimentally
247 (Bendix et al., 2008). For buckling to happen, the crosslinking density must be high enough to sustain the
248 forces exerted by the myosin motors while buckling the filaments. Therefore, we expect the boundary
249 between the filament buckling or the polarity sorting mechanisms to be determined by the ratio of end-
250 dwelling myosins to crosslinkers. On the diagram where the two concentrations are varied, the regions
251 dominated by either mechanism are thus separated along a diagonal (Fig. 7c, d).

252 The above results highlight the prominent role of polarity-sorting in the contraction of networks that
253 resemble the *in vitro* conditions reported in our experiments. In physiological conditions, for example in
254 the cortex of animal cells, the actin filaments are about one order of magnitude shorter than in our *in*
255 *vitro* systems (about 1 µm or less (Fritzsche et al., 2016)), and the mesh size is also much shorter
256 (between 0.03 to 0.1 µm (Bovellan et al., 2014; Fujiwara et al., 2016)). One can thus expect polarity-
257 sorting to be even more critical in the cortex for two reasons: Firstly, the force required to buckle a
258 filament segment increases with the inverse of the squared length of the segment, and thus becomes
259 greater as the mesh size is reduced. Secondly, the ratio of end-dwelling versus side-bound motors would
260 also increase as the filaments become shorter. To assess these effects, we performed simulations with
261 denser networks made of shorter filaments that better resemble the actomyosin cortex and varied the
262 concentrations of myosin and α-actinin as before (Fig. 8a). With these conditions, most of the networks
263 contract to a single aster rather than multiple ones, probably because they are more tightly connected.
264 When the end-dwelling property of myosin is turned off, the contractile behavior is lost in a region of the
265 phase diagram that is similar to the region that lost contractions under the simulated conditions of the *in*
266 *vitro* experiments (Fig. 7c, d). However, a significant number of networks with low myosin and high α-
267 actinin concentrations are now stalled, whereas they were contractile under the buckling mechanism at
268 lower density. Therefore, under conditions mimicking the actin cortex *in vivo*, the effectiveness of the
269 buckling mechanism is reduced, while polarity sorting is preserved. Note that for low α-actinin
270 concentrations, filaments freely glide over the network, powered by the myosin motors. In these

bioRxiv preprint doi: https://doi.org/10.1101/314484; this version posted May 4, 2018. The copyright holder for this preprint (which was not certified by peer review) is the author/funder. All rights reserved. No reuse allowed without permission.

271 conditions, filaments are pushed out of the initial geometry more readily, due to the smaller overall
272 available space, and the effect is more visible compared to the *in vitro*-like simulations (Fig. 7d). These
273 results confirm that the polarity sorting mechanism remains effective when the characteristics of the
274 actomyosin networks are more cortex-like, while at the same time the buckling-mediated mechanisms
275 decreases in importance.

276 ## Discussion

277 An important biological function of actin-myosin networks is their contractility, for which the underlying
278 mechanism is still not fully understood. Here we show that myosin motors remodel initially random actin
279 networks into polarized domains. Using low protein densities to observe actin-myosin interactions at the
280 single filament level, we identify myosin dwelling at actin filament ends as the mechanism for this
281 polarity sorting. Our study thus reveals how contractile nodes, which are often assumed in theoretical
282 studies of actin-myosin networks, form by self-organization (Alvarado et al., 2013; Hannezo et al., 2015;
283 Jülicher et al., 2007; Salbreux et al., 2009). We find that aster formation occurs over a wide range of
284 crosslinker and myosin densities. At low crosslink densities that are below the percolation threshold, the
285 asters are relatively small and transient. At crosslink densities above the percolation threshold, the
286 asters are stabilized and neighboring asters pull on each other over long distances and merge, leading to
287 large-scale contraction. The crucial role for crosslinkers to tune the range of force transmission is in line
288 with prior experimental and theoretical work (Alvarado et al., 2013; Bendix et al., 2008; Chugh et al.,
289 2017; Vavylonis et al., 2008). But we find that crosslinkers favor contraction not only by providing elastic
290 connections but also by allowing formation of stable F-actin bundle tracks that promote inward transport
291 of myosin to form large and stable asters. By contrast, in the absence of crosslinkers, myosin clusters are
292 dynamic and split because myosin filaments can switch between different actin filament tracks. Asters
293 are also observed over a range of motor densities, in conditions of stalled networks (low motor density),
294 globally contracting networks (intermediate motor density), and local contraction (high motor density).
295 These contractile behaviors are reproduced in simulations, where we can directly compare the
296 remodeling effect of motors with and without end-dwelling. The simulations demonstrate that end-
297 dwelling is an important requirement for network contraction while contraction due to filament buckling
298 only happens for a limited set of parameters

299 In our study we use skeletal muscle myosin-2 filaments. While muscle myosin is used in nearly all
300 reconstituted actomyosin systems thus far, with few exceptions (Thoresen et al., 2013), contraction in
301 other cells is driven by non-muscle myosins. These differ from skeletal muscle myosin 2 in their kinetic
302 properties and the formation of much smaller bipolar filament ensembles of only 10-20 motors
303 (Erdmann et al., 2016). Clearly, in future it will be interesting to study if end-dwelling is also observed for
304 non-muscle myosin. Our results suggest that the dwelling behavior is mainly mediated by the trailing end
305 of the myosin filaments. While non-muscle myosin filaments are reported to be much shorter than
306 skeletal muscle myosin filaments (Billington et al., 2013), their longer duty ratio might compensate and
307 still permit end-dwelling (Kovács et al., 2003; Wang et al., 2003). Possibly the ratio between the two
308 major non-muscle myosin isoforms, NMMII A and B, could also play a role in the stability of filament end-
309 dwelling (Melli et al., 2017).

bioRxiv preprint doi: https://doi.org/10.1101/314484; this version posted May 4, 2018. The copyright holder for this preprint (which was not certified by peer review) is the author/funder. All rights reserved. No reuse allowed without permission.

310 We show that myosin-driven polarity sorting can be an efficient mechanism for actomyosin network
311 contraction provided that enough crosslinkers are present to allow force transmission. Prior studies of
312 reconstituted actin-myosin networks showed that in the presence of crosslinkers, motor-mediated
313 buckling of actin filaments can provide the dominant mechanism for contraction, sometimes augmented
314 by severing of buckled actin filaments (Murrell and Gardel, 2012). But both our experimental and
315 computational findings suggest that even in crosslinked networks, there is still an underlying tendency
316 for actin and myosin to form polarity-sorted structures. The relative contributions of polarity sorting
317 versus buckling to the overall network contraction depend on microscopic parameters such as the
318 distance between crosslinks, the motor density, and whether actin filaments are bundled. A full
319 characterization of these parameters is beyond the scope of this study. Simple scaling considerations
320 indicate that buckling may be disfavored in the *in vivo* actin cortex. First, recent work suggests that the
321 actin cortex is composed of filaments that are relatively short, being a mixture of formin-nucleated
322 filaments with lengths on the order of 1 µm, and Arp2/3-nucleated filaments in the 100 nm range
323 (Fritzsche et al., 2016). Second, electron microscopy images revealed typical cortical mesh sizes of only
324 30 to 200 nm, which might correspond to the distance between crosslinkers (Bovellan et al., 2014;
325 Fujiwara et al., 2016). These characteristics would make buckling difficult, but leave polarity sorting as a
326 potent contraction mechanism, as our *in silico* study showed.

327 There are some reports of actin polarity sorting in a few cellular structures by electron microscopy (Begg
328 et al., 1978; Cramer et al., 1997; Kamasaki et al., 2007; Sanger and Sanger, 1980). Furthermore, myosin
329 foci are commonly observed in the actin cortex of cells and early embryos. However, the cell cortex is
330 mainly regarded as a random actin network. Recent theoretical studies of contractile networks with actin
331 turnover suggest that the absence of asters in the cell cortex may be due to turnover (Guthardt Torres et
332 al., 2010; McFadden et al., 2017). Consistent with this idea, asters can be formed in the actin cortex if
333 actin polymerization is reduced or blocked by drugs (Luo et al., 2013; Verkhovsky et al., 1997), and actin
334 stabilization seems to have a similar effect (Wehland et al., 1977). We therefore speculate that polarity
335 sorting may occur in cortical actin networks but that actin turnover prevents formation of large polar
336 domains. Moreover, polarity sorting may be counteracted by other remodeling processes such as Arp2/3
337 nucleator-dependent self-organization (Fritzsche et al., 2017) and biochemical feedback between active
338 RhoA and myosin (Nishikawa et al., 2017). New developments in high resolution microscopy will
339 hopefully enable the visualization of local accumulation of actin plus ends in the cortex or other
340 contractile structures such as the cytokinetic ring, and thereby lead to a better understanding of the role
341 of polarity sorting in cells (Hu et al., 2017).

342

343

344

345

bioRxiv preprint doi: https://doi.org/10.1101/314484; this version posted May 4, 2018. The copyright holder for this preprint (which was not certified by peer review) is the author/funder. All rights reserved. No reuse allowed without permission.

346 # Materials and Methods
347

348 **Protein preparation**

349 Actin and myosin are purified from rabbit muscle as described previously (Alvarado and Koenderink,
350 2015). Myosin is labelled with Alexa Fluor 488 NHS ester (Invitrogen). Actin is labelled with Alexa Fluor
351 649 carboxylic acid, succinimidyl ester. The crosslinker protein α-actinin-1 in unlabeled form and tagged
352 with mCherry is purified as described in (Ciobanasu et al., 2014). Myosin is stored in myosin buffer (300
353 mM KCl, 4 mM $MgCl_2$, 20 mM imidazole, 1 mM dithiothreitol (DTT)) with 50% glycerol. Prior to the
354 experiment, myosin is dialyzed overnight against the myosin buffer to remove the glycerol. At this salt
355 concentration myosin does not self-assemble into filaments. Actin is stored in G-Buffer (2 mM Tris-HCl,
356 0.2 mM ATP, 0.2 mM $CaCl_2$, 0.2 mM DTT) in its monomeric (G-actin) form.

357 **Chamber preparation**

358 Glass coverslips are cleaned with base piranha for 10 min(Alvarado and Koenderink, 2015) and
359 thoroughly rinsed with milliQ water. A homemade silicone sheet with 9mm^2 holes is placed on top of the
360 glass coverslip to build open chambers. In some experiments (Table 1, supplementary information),
361 classical flow cells are used similar to the ones described in (Alvarado and Koenderink, 2015). The
362 surfaces are passivated with lipid bilayers: small unilamellar vesicles (SUVs, see below) are flushed into
363 the chamber. After an incubation time of at least 5 min, excess vesicles are flushed out with F-buffer (50
364 mM KCl, 2 mM $MgCl_2$, 20 mM imidazole). To prevent drying between flushing steps, the chamber is kept
365 in a humid atmosphere.

366 **SUV preparation**

367 Lipids are stored in chloroform. To remove chloroform, lipid solution (typically 50 µl) is pipetted into a
368 glass tube. Chloroform is slowly evaporated by gentle nitrogen flow while turning the tilted glass tube to
369 achieve a homogenous layer of lipids at the bottom of the tube. To remove any remaining chloroform,
370 the tube is kept in vacuum overnight. The lipids are resuspended in buffer (20 mM imidazole, 50 mM KCl)
371 and sonicated with a tip sonicator for 30 min to make small unilamellar vesicles (SUVs). We use 1.9
372 mg/ml of the neutral lipid DOPC (1,2-dioleoyl-sn- glycero-3-phosphocholine, Avanti Polar Lipids). For
373 open chamber experiments we supplement the membrane with 1 mol% of PEGylated lipids PEG-PE (1,2-
374 dipalmitoyl-sn-glycero-3- phosphoethanolamine-N-[methoxy(polyethylene glycol)-2000], Avanti Polar
375 Lipids) to make the bilayer more resilient against drying.

376 **Contraction experiment**

377 In the cases where we use an open chamber, actin is prepolymerized for longer than 1h. Myosin is then
378 added with the contraction buffer (50 mM KCl, 2 mM $MgCl_2$, 20 mM imidazole, 1 mM DTT, 0.1 mM ATP,
379 2 mM protocatechuic acid (PCA), 0.1 µM protocatechuase 3,4-dioxygenase (PCD), 10 mM creatine
380 phosphate (CP), 0.1 mg/ml creatine kinase (CK), 0.3 % methyl cellulose (MC)). CP and CK are used as an
381 ATP replenishing system, while PCA and PCD are used as an oxygen scavenger system and MC acts as a

bioRxiv preprint doi: https://doi.org/10.1101/314484; this version posted May 4, 2018. The copyright holder for this preprint (which was not certified by peer review) is the author/funder. All rights reserved. No reuse allowed without permission.

382 crowding agent that pushes actin and myosin filaments towards the coverslip. In flow cell experiments,
383 monomeric actin is mixed with the contraction buffer, which triggers its polymerization, and the mix is
384 immediately injected into the channel. Exact actin and myosin concentrations can be found in Table 1 of
385 the supplementary information.

386 **Diluted filament assay**

387 Diluted filament conditions shown in Fig. 2 to 4 are obtained either by polymerizing actin is at low
388 concentrations or by slowing down polymerization of an initially dense actin solution by diluting after a
389 few minutes. The exact conditions can be found in Table 1 of the supplementary information. Myosin is
390 added to the filaments in the contraction buffer. For experiments where myosin activity is triggered by
391 addition of ATP solution to a final concentration of 0.1 mM (Fig. 2a), the contraction buffer does not
392 contain ATP.

393 **Microscopy and image analysis**

394 Confocal images were taken with a Nikon Eclipse Ti inverted microscope equipped with a Nikon C1
395 confocal scan head and a 100-mW Argon ion laser (488 nm, 561 nm, Coherent, CA), or with a Nikon
396 Eclipse Ti inverted microscope equipped with a CrEST spinning disk unit, a solid state light source
397 (SpectraX, Lumencor, OR) and a Hamamatsu camera. Typical exposure time was 200 ms. Total internal
398 reflection fluorescence (TIRF) imaging was performed with a Nikon Eclipse Ti-E inverted microscope
399 equipped with a Roper TIRF module and QuantEM:512SC EMCCD camera. Exposure time was 100 ms.

400 Image analysis was performed with the ImageJ distribution Fiji (Schindelin et al., 2012; Schneider et al.,
401 2012). The intensity background was subtracted with Fiji. For representation purposes images were
402 smoothened. The velocity of myosin filament motion on actin filaments (Fig. 1c and 2b) was measured by
403 manual tracking of single myosin filaments using the "Manual Tracking" plugin of ImageJ. Temporal
404 overlays (Fig. 6, Suppl. Fig. 4) were made with the ImageJ plugin "Temporal-Color Coder". Kymographs
405 were made with Fiji. To detect myosin and actin filament edges (Fig. 3), we took line profiles of the
406 respective fluorescence signals. The edge position was determined as the maximum in the first derivative
407 of the profiles.

408 **Electron microscopy**

409 Transmission electron microscopy images were taken with a FEI Verios 460. Myosin was assembled in F-
410 Buffer at 0.2 µM. The solution was diluted (typically 1:100), applied on an electron microscopy grid (300
411 mesh Cu grid, Ted Pella inc., CA), and rinsed with ultrapure water after 1 min of incubation. Finally the
412 grid was air dried. Myosin length measurements were performed manually with the ImageJ distribution
413 Fiji (Schindelin et al., 2012; Schneider et al., 2012).

414 **Computer Simulations**

415 The simulations of contractile actin-myosin networks were performed with the Open Source software
416 Cytosim (github.com/nedelec/cytosim), which uses a Brownian dynamics approach as described
417 previously (Nedelec and Foethke, 2007). Actin filaments are modeled as incompressible bendable

bioRxiv preprint doi: https://doi.org/10.1101/314484; this version posted May 4, 2018. The copyright holder for this preprint (which was not certified by peer review) is the author/funder. All rights reserved. No reuse allowed without permission.

418 filaments of rigidity 0.075 pN.µm^2 (corresponding to a persistence length of 18 µm) in a medium of 419 viscosity 0.18 Pa.s. The α-actinin crosslinkers are modeled as Hookean springs of zero resting length and 420 a rigidity of 50 pN/µm, with a binding rate k_{on} = 15 s^{-1}, a binding range of 0.02 µm and a slip-bond 421 unbinding model: $k_{off} = k_{off,0} \exp(-|f|/f_0)$ with a basal unbinding rate of $k_{off,0}$ = 0.3 s^{-1} and unbinding force 422 of f_0 = 2 pN. Myosin mini-filaments were modeled as an inextensible 1D object of length 0.8 µm with 4 423 motors on each side spaced by 0.08 µm from the extremities. Motors operate independently from each 424 other and also behave as a Hookean spring when attached to an actin filament, with zero resting length 425 and a rigidity of 100 pN/µm. Additionally motors move on filaments with a speed of 2 µm/s, with a linear 426 force-velocity relationship characterized by a stall force of 4 pN. Each motor has a binding rate of k_{on} = 10 427 s^{-1}, a binding range of 0.01 µm and a force-independent unbinding rate of k_{off} = 0.5 s^{-1}. Unless otherwise 428 specified, motors end-dwell by stopping upon reaching the end of filaments without changing their 429 unbinding rates. Motors and α-actinin binding and unbinding events are modeled as first-order 430 stochastic processes and we neglected steric interaction between filaments, motors and crosslinkers.

431 The simulations without α-actinin (Fig. 7a-c) were done with 200 actin filaments randomly distributed 432 over a square area of 40x40 µm^2, with filament lengths following an exponential distribution with a 433 mean of 10 µm that was truncated inside [0.5; 20] µm. For the simulations reproducing the *in vitro*-like 434 conditions (Fig. 7d,e), 800 actin filaments were randomly distributed over a square area of 80x80 µm^2, 435 with filaments lengths distribution as before. In those simulations the resulting mesh-size (measured as 436 the average distance between consecutive filament crossings) was about 1.1 µm. For the simulations 437 that reproduce the cortex-like conditions, 3500 filaments were randomly distributed over a square area 438 of 8x8 µm^2, with exponentially distributed lengths, with a mean of 1 µm truncated in [0.1; 4] µm. The 439 resulting mesh-size was about 0.1 µm. In both scenarios the filaments are mixed with varying amounts of 440 α-actinin crosslinkers and myosin mini-filaments. The concentrations of myosin and α-actinin are defined 441 as number of elements per total length of actin (units of µm^{-1}) and were varied within the ranges [0.1:6.4 442 µm^{-1}] and [1:64 µm^{-1}], respectively, for both scenarios. To better mimic experimental conditions, actin 443 filaments are not created as straight filaments, but already relaxed according to their persistence length 444 (18 µm), and the simulations start with all motors and crosslinkers unbound. The reference configuration 445 files for each scenarios are provided as Supplementary File.

446 In the phase diagrams (Figs. 7d,e and 8a,b), the boundary between the Polarity Sorting (PS) and Filament 447 Buckling (FB) mechanisms was determined by comparing the contraction rates of the with and without 448 end-dwelling. The contraction rates were calculated as in (Belmonte et al., 2017). The regions of the 449 phase diagram where 50% or more of the contraction is lost when end-dwelling is turned off were 450 considered to be dominated by the Polarity Sorting mechanism. The boundary line is estimated by 451 creating a matrix with the normalized difference in contraction between the simulations with and 452 without end-dwelling, which was later smoothed using a 2D boxcar average with window size of 3. We 453 then used the matplotlib library from python to calculate the isocline at 0.5. The networks that 454 experience a small initial contraction (10 % or less) that stopped after a few seconds were considered to 455 be non-contractile and made the Stalled (S) region of the phase diagrams of Fig. 8. Note that the 456 networks in same region of the phase diagrams in Fig. 7 experience a slow but continuous contraction, 457 and therefore were not considered stalled.

bioRxiv preprint doi: https://doi.org/10.1101/314484; this version posted May 4, 2018. The copyright holder for this preprint (which was not certified by peer review) is the author/funder. All rights reserved. No reuse allowed without permission.

458 ## Acknowledgements

459 This work is part of the research program of the Netherlands Organisation for Scientific Research (NWO)
460 and was financially supported by an ERC Starting Grant (335672-MINICELL). We thank Dr. C. Le Clainche
461 (Institute for Integrative Biology of the Cell (I2BC), Université Paris-Sud) for kindly providing the α-
462 actinin-1 constructs and Marjolein Vinkenoog-Kuit for protein purification. FJN is supported by the
463 Center for Modelling and Simulation in the Biosciences (BioMS). JMB and ML are supported by EMBO
464 and EMBL. We wish to acknowledge EMBL IT support.

465

466 ## References

467

468 Akhmanova, A., and Hoogenraad, C.C. (2005). Microtubule plus-end-tracking proteins: Mechanisms and
469 functions. Curr. Opin. Cell Biol. *17*, 47–54.

470 Alvarado, J., and Koenderink, G.H. (2015). Reconstituting cytoskeletal contraction events with
471 biomimetic actin e myosin active gels. In Methods in Cell Biology, pp. 83–103.

472 Alvarado, J., Sheinman, M., Sharma, A., MacKintosh, F.C., and Koenderink, G.H. (2013). Molecular motors
473 robustly drive active gels to a critically connected state. Nat. Phys. *9*, 591–597.

474 Alvarado, J., Sheinman, M., Sharma, A., MacKintosh, F.C., and Koenderink, G.H. (2017). Force percolation
475 of contractile active gels. Soft Matter *13*, 5624–5644.

476 Backouche, F., Haviv, L., Groswasser, D., and Bernheim-Groswasser, A. (2006). Active gels: dynamics of
477 patterning and self-organization. Phys. Biol. *3*, 264–273.

478 Begg, D.A., Rodewald, R., and Rebhun, L.I. (1978). The Visualization of actin filaments in thin sections. J.
479 Cell Biol. *79*, 846–852.

480 Belmonte, J.M., Leptin, M., and Nédélec, F. (2017). A theory that predicts behaviors of disordered
481 cytoskeletal networks. Mol. Syst. Biol. *13*, 941.

482 Bendix, P.M., Koenderink, G.H., Cuvelier, D., Dogic, Z., Koeleman, B.N., Brieher, W.M., Field, C.M.,
483 Mahadevan, L., and Weitz, D.A. (2008). A Quantitative Analysis of Contractility in Active Cytoskeletal
484 Protein Networks. Biophys. J. *94*, 3126–3136.

485 Billington, N., Wang, A., Mao, J., Adelstein, R.S., and Sellers, J.R. (2013). Characterization of three full-
486 length human nonmuscle myosin II paralogs. J. Biol. Chem. *288*, 33398–33410.

487 Biro, M., Romeo, Y., Kroschwald, S., Bovellan, M., Boden, A., Tcherkezian, J., Roux, P.P., Charras, G., and
488 Paluch, E.K. (2013). Cell cortex composition and homeostasis resolved by integrating proteomics and
489 quantitative imaging. Cytoskeleton *70*, 741–754.

490 Blanchoin, L., Boujemaa-paterski, R., Sykes, C., and Plastino, J. (2014). Actin dynamics, architecture, and
491 mechanics in cell motility. 235–263.

bioRxiv preprint doi: https://doi.org/10.1101/314484; this version posted May 4, 2018. The copyright holder for this preprint (which was not certified by peer review) is the author/funder. All rights reserved. No reuse allowed without permission.

492 Bovellan, M., Romeo, Y., Biro, M., Boden, A., Chugh, P., Yonis, A., Vaghela, M., Fritzsche, M., Moulding,
493 D., Thorogate, R., et al. (2014). Cellular control of cortical actin nucleation. Curr. Biol. *24*, 1628–1635.

494 Chugh, P., Clark, A.G., Smith, M.B., Cassani, D.A.D., Dierkes, K., Ragab, A., Roux, P.P., Charras, G.,
495 Salbreux, G., and Paluch, E.K. (2017). Actin cortex architecture regulates cell surface tension. Nat. Cell
496 Biol. *19*, 689–697.

497 Ciobanasu, C., Faivre, B., and Le Clainche, C. (2014). Actomyosin-dependent formation of the
498 mechanosensitive talin-vinculin complex reinforces actin anchoring. Nat. Commun. *5*, 3095.

499 Cramer, L.P., Siebert, M., and Mitchison, T.J. (1997). Identification of novel graded polarity actin filament
500 bundles in locomoting heart fibroblasts: Implications for the generation of motile force. J. Cell Biol. *136*,
501 1287–1305.

502 Eghiaian, F., Rigato, A., and Scheuring, S. (2015). Structural, mechanical, and dynamical variability of the
503 actin cortex in living cells. Biophys. J. *108*, 1330–1340.

504 Ennomani, H., Letort, G., Guérin, C., Martiel, J.L., Cao, W., Nédélec, F., De La Cruz, E.M., Théry, M., and
505 Blanchoin, L. (2016). Architecture and Connectivity Govern Actin Network Contractility. Curr. Biol. *26*,
506 616–626.

507 Erdmann, T., Bartelheimer, K., and Schwarz, U.S. (2016). Sensitivity of small myosin II ensembles from
508 different isoforms to mechanical load and ATP concentration. Phys. Rev. E - Stat. Nonlinear, Soft Matter
509 Phys. *94*, 1–9.

510 Field, C.M., and Lénárt, P. (2011). Bulk cytoplasmic actin and its functions in meiosis and mitosis. Curr.
511 Biol. *21*, 825–830.

512 Foster, P.J., Furthauer, S., Shelley, M.J., and Needleman, D.J. (2015). Active contraction of microtubule
513 networks. 1–21.

514 Fritzsche, M., Erlenkämper, C., Moeendarbary, E., Charras, G., and Kruse, K. (2016). Actin kinetics shapes
515 cortical network structure and mechanics. Sci. Adv. 1–13.

516 Fritzsche, M., Li, D., Colin-York, H., Chang, V.T., Moeendarbary, E., Felce, J.H., Sezgin, E., Charras, G.,
517 Betzig, E., and Eggeling, C. (2017). Self-organizing actin patterns shape membrane architecture but not
518 cell mechanics. Nat. Commun. *8*, 14347.

519 Fujiwara, T.K., Iwasawa, K., Kalay, Z., Tsunoyama, T.A., Watanabe, Y., Umemura, Y.M., Murakoshi, H.,
520 Suzuki, K.G.N., Nemoto, Y.L., Morone, N., et al. (2016). Confined diffusion of transmembrane proteins
521 and lipids induced by the same actin meshwork lining the plasma membrane. Mol. Biol. Cell *27*, 11–81.

522 Gautel, M., and Djinovic-Carugo, K. (2016). The sarcomeric cytoskeleton: from molecules to motion. J.
523 Exp. Biol. *219*, 135–145.

524 Guthardt Torres, P., Doubrovinski, K., and Kruse, K. (2010). Filament turnover stabilizes contractile
525 cytoskeletal structures. Europhys. Lett. *91*, 68003.

526 Hannezo, E., Dong, B., Recho, P., Joanny, J.-F., and Hayashi, S. (2015). Cortical instability drives periodic
527 supracellular actin pattern formation in epithelial tubes. Proc. Natl. Acad. Sci. *112*, 8620–5.

528 Harris, D.E., and Warshaw, D.M. (1993). Smooth and skeletal muscle myosin both exhibit low duty cycles

bioRxiv preprint doi: https://doi.org/10.1101/314484; this version posted May 4, 2018. The copyright holder for this preprint (which was not certified by peer review) is the author/funder. All rights reserved. No reuse allowed without permission.

529 at zero load in vitro. J. Biol. Chem. *268*, 14764–14768.

530 Hu, S., Dasbiswas, K., Guo, Z., Tee, Y., Thiagarajan, V., Hersen, P., Chew, T., Safran, S.A., Zaidel-bar, R.,
531 and Bershadsky, A.D. (2017). Long-range self-organization of cytoskeletal myosin II filament stacks. Nat.
532 Cell Biol. *19*, 133.

533 Jülicher, F., Kruse, K., Prost, J., and Joanny, J.-F. (2007). Active behavior of the Cytoskeleton. Phys. Rep.
534 *449*, 3–28.

535 Kamasaki, T., Osumi, M., and Mabuchi, I. (2007). Three-dimensional arrangement of F-actin in the
536 contractile ring of fission yeast. J. Cell Biol. *178*, 765–771.

537 Kang, H., Bradley, M.J., McCullough, B.R., Pierre, A., Grintsevich, E.E., Reisler, E., and De La Cruz, E.M.
538 (2012). Identification of cation-binding sites on actin that drive polymerization and modulate bending
539 stiffness. PNAS *109*, 16923–16927.

540 Koenderink, G.H., Dogic, Z., Nakamura, F., Bendix, P.M., MacKintosh, F.C., Hartwig, J.H., Stossel, T.P., and
541 Weitz, D.A. (2009). An active biopolymer network controlled by molecular motors. Proc. Natl. Acad. Sci.
542 *106*, 15192–15197.

543 Köhler, S., Schaller, V., and Bausch, A.R. (2011). Structure formation in active networks. Nat. Mater.

544 Köster, D.V., Husain, K., Iljazi, E., Bhat, A., Bieling, P., Mullins, R.D., Rao, M., and Mayor, S. (2016).
545 Actomyosin dynamics drive local membrane component organization in an in vitro active composite
546 layer. Proc. Natl. Acad. Sci. *113*, E1645–E1654.

547 Kovács, M., Wang, F., Hu, A., Zhang, Y., and Sellers, J.R. (2003). Functional divergence of human
548 cytoplasmic myosin II. Kinetic characterization of the non-muscle IIA isoform. J. Biol. Chem. *278*, 38132–
549 38140.

550 Kruse, K., and Jülicher, F. (2000). Actively contracting bundles of polar filaments. Phys. Rev. Lett. *85*,
551 1778–1781.

552 Laporte, D., Ojkic, N., Vavylonis, D., and Wu, J.-Q. (2012). α-Actinin and fimbrin cooperate with myosin II
553 to organize actomyosin bundles during contractile-ring assembly. Mol. Biol. Cell *23*, 3094–3110.

554 Lenz, M., Thoresen, T., Gardel, M.L., and Dinner, A.R. (2012). Contractile Units in Disordered Actomyosin
555 Bundles Arise from F-Actin Buckling. Phys. Rev. Lett. *108*, 238107.

556 Linsmeier, I., Banerjee, S., Oakes, P.W., Jung, W., Kim, T., and Murrell, M.P. (2016). Disordered
557 actomyosin networks are sufficient to produce cooperative and telescopic contractility. Nat. Commun. *7*,
558 12615.

559 Lu, W., Fox, P., Lakonishok, M., Davidson, M.W., and Gelfand, V.I. (2013). Initial neurite outgrowth in
560 drosophila neurons is driven by kinesin-powered microtubule sliding. Curr. Biol. *23*, 1018–1023.

561 Luo, W., Yu, C.-H., Lieu, Z.Z., Allard, J., Mogilner, A., Sheetz, M.P., and Bershadsky, A.D. (2013). Analysis of
562 the local organization and dynamics of cellular actin networks. J. Cell Biol. *202*, 1057–1073.

563 Mackintosh, F.C., and Levine, A.J. (2008). Nonequilibrium mechanics and dynamics of motor-activated
564 gels. Phys. Rev. Lett. *100*, 1–4.

bioRxiv preprint doi: https://doi.org/10.1101/314484; this version posted May 4, 2018. The copyright holder for this preprint (which was not certified by peer review) is the author/funder. All rights reserved. No reuse allowed without permission.

565 McFadden, W.M., McCall, P.M., Gardel, M.L., and Munro, E.M. (2017). Filament turnover tunes both
566 force generation and dissipation to control long- range flows in a model actomyosin cortex. PLoS
567 Comput. Biol. *13*, 1–27.

568 Melli, L., Billington, N., Sun, S.A., Bird, J., Nagy, A., Friedman, T.B., Takagi, Y., and Sellers, J.R. (2017).
569 Bipolar filaments of human nonmuscle myosin 2-A and 2-B have distinct motile and mechanical
570 properties. BioRxiv 207514.

571 Mendes Pinto, I., Rubinstein, B., Kucharavy, A., Unruh, J.R., and Li, R. (2012). Actin Depolymerization
572 Drives Actomyosin Ring Contraction during Budding Yeast Cytokinesis. Dev. Cell *22*, 1247–1260.

573 Murrell, M., and Gardel, M.L. (2014). Actomyosin Sliding is Attenuated in Contractile Biomimetic
574 Cortices. Mol. Biol. Cell *25*, 1845–1853.

575 Murrell, M.P., and Gardel, M.L. (2012). F-actin buckling coordinates contractility and severing in a
576 biomimetic actomyosin cortex. Proc. Natl. Acad. Sci. U. S. A. *109*, 20820–20825.

577 Murrell, M., Oakes, P.W., Lenz, M., and Gardel, M.L. (2015). Forcing cells into shape: the mechanics of
578 actomyosin contractility. Nat. Rev. Mol. Cell Biol.

579 Naumanen, P., Lappalainen, P., and Hotulainen, P. (2008). Mechanisms of actin stress fibre assembly. J.
580 Microsc. *231*, 446–454.

581 Nédélec, F., and Foethke, D. (2007). Collective Langevin dynamics of flexible cytoskeletal fibers. New J.
582 Phys. *9*, 427.

583 Nishikawa, M., Naganathan, S.R., Jülicher, F., and Grill, S.W. (2017). Controlling contractile instabilities in
584 the actomyosin cortex. Elife *6*, 1–21.

585 Ojkic, N., Wu, J.-Q., and Vavylonis, D. (2011). Model of myosin node aggregation into a contractile ring:
586 the effect of local alignment. J. Phys. Condens. Matter *23*, 374103.

587 Ronceray, P., Broedersz, C., and Lenz, M. (2015). Fiber networks amplify active stress. 1–8.

588 Ronceray, P., Broedersz, C.P., and Lenz, M. (2016). Fiber networks amplify active stress. Proc. Natl. Acad.
589 Sci. *113*, 2827–2832.

590 Salbreux, G., Prost, J., and Joanny, J.-F. (2009). Hydrodynamics of Cellular Cortical Flows and the
591 Formation of Contractile Rings. Phys. Rev. Lett. *103*, 058102.

592 Salbreux, G., Charras, G., and Paluch, E. (2012). Actin cortex mechanics and cellular morphogenesis.
593 Trends Cell Biol. *22*, 536–45.

594 Sanchez, T., Chen, D.T.N., DeCamp, S.J., Heymann, M., and Dogic, Z. (2012). Spontaneous motion in
595 hierarchically assembled active matter. Nature *491*, 431–434.

596 Sanger, J.M., and Sanger, J.W. (1980). Banding and polarity of actin filaments in interphase and cleaving
597 cells. J. Cell Biol. *86*, 568–575.

598 Schindelin, J., Arganda-Carreras, I., Frise, E., Kaynig, V., Longair, M., Pietzsch, T., Preibisch, S., Rueden, C.,
599 Saalfeld, S., Schmid, B., et al. (2012). Fiji: an open-source platform for biological-image analysis. Nat.
600 Methods *9*, 676–682.

bioRxiv preprint doi: https://doi.org/10.1101/314484; this version posted May 4, 2018. The copyright holder for this preprint (which was not certified by peer review) is the author/funder. All rights reserved. No reuse allowed without permission.

601 Schneider, C.A., Rasband, W.S., and Eliceiri, K.W. (2012). NIH Image to ImageJ: 25 years of image analysis.
602 Nat. Methods *9*, 671–675.

603 Sellers, J.R., and Kachar, B. (1990). Polarity and velocity of sliding filaments: control of direction by actin
604 and of speed by myosin. Science *249*, 406–408.

605 Soares e Silva, M., Depken, M., Stuhrmann, B., Korsten, M., MacKintosh, F.C., and Koenderink, G.H.
606 (2011). Active multistage coarsening of actin networks driven by myosin motors. Proc. Natl. Acad. Sci.
607 *108*, 9408–9413.

608 Stam, S., Freedman, S.L., Banerjee, S., Weirich, K.L., Dinner, A.R., and Gardel, M.L. (2017). Filament
609 rigidity and connectivity tune the deformation modes of active biopolymer networks. Proc. Natl. Acad.
610 Sci. 201708625.

611 Surrey, T., Nédélec, F., Leibler, S., and Karsenti, E. (2001). Physical properties determining self-
612 organization of motors and microtubules. Science (80-.). *292*, 1167–1171.

613 Tan, R., Foster, P.J., Needleman, D.J., and McKenney, R.J. (2018). Cooperative Accumulation of Dynein-
614 Dynactin at Microtubule Minus-Ends Drives Microtubule Network Reorganization. Dev. Cell *44*, 233–247.

615 Thoresen, T., Lenz, M., and Gardel, M.L. (2013). Thick filament length and isoform composition
616 determine self-organized contractile units in actomyosin bundles. Biophys. J. *104*, 655–665.

617 Torisawa, T., Taniguchi, D., Ishihara, S., and Oiwa, K. (2016). Spontaneous Formation of a Globally
618 Connected Contractile Network in a Microtubule-Motor System. Biophys. J. *111*, 373–385.

619 Vavylonis, D., Wu, J.-Q., Hao, S., O'Shaughnessy, B., and Pollard, T.D. (2008). Assembly mechanism of the
620 contractile ring for cytokinesis by fission yeast. Science (80-.). *319*, 97–100.

621 Verkhovsky, A.B., Svitkina, T.M., and Borisy, G.G. (1997). Polarity sorting of actin filaments in
622 cytochalasin-treated fibroblasts. J. Cell Sci. *1704*, 1693–1704.

623 Vogel, S.K., Petrasek, Z., Heinemann, F., and Schwille, P. (2013). Myosin motors fragment and compact
624 membrane-bound actin filaments. Elife *2*, e00116.

625 Wang, F., Kovacs, M., Hu, A., Limouze, J., Harvey, E. V, and Sellers, J.R. (2003). Kinetic mechanism of non-
626 muscle myosin IIB: functional adaptations for tension generation and maintenance. J. Biol. Chem. *278*,
627 27439–27448.

628 Wehland, J., Osborn, M., and Weber, K. (1977). Phalloidin-induced actin polymerization in the cytoplasm
629 of cultured cells interferes with cell locomotion and growth. Proc. Natl. Acad. *74*, 5613–5617.

630 Wollrab, V., Thiagarajan, R., Wald, A., Kruse, K., and Riveline, D. (2016). Still and rotating myosin clusters
631 determine cytokinetic ring constriction. Nat. Commun. *7*, 1–9.

632 Yamada, A., and Wakabayashi, T. (1993). Movement of actin away from the center of reconstituted
633 rabbit myosin filament is slower than in the opposite direction. Biophys. J. *64*, 565–569.

634 Zaidel-Bar, R., Zhenhuan, G., and Luxenburg, C. (2015). The contractome - a systems view of actomyosin
635 contractility in non-muscle cells. J. Cell Sci. *128*, 2209–2217.

636 Zumdieck, A., Kruse, K., Bringmann, H., Hyman, A.A., and Jülicher, F. (2007). Stress generation and

bioRxiv preprint doi: https://doi.org/10.1101/314484; this version posted May 4, 2018. The copyright holder for this preprint (which was not certified by peer review) is the author/funder. All rights reserved. No reuse allowed without permission.

637 filament turnover during actin ring constriction. PLoS One *2*, e696.

638

bioRxiv preprint doi: https://doi.org/10.1101/314484; this version posted May 4, 2018. The copyright holder for this preprint (which was not certified by peer review) is the author/funder. All rights reserved. No reuse allowed without permission.

639 # Figures

640

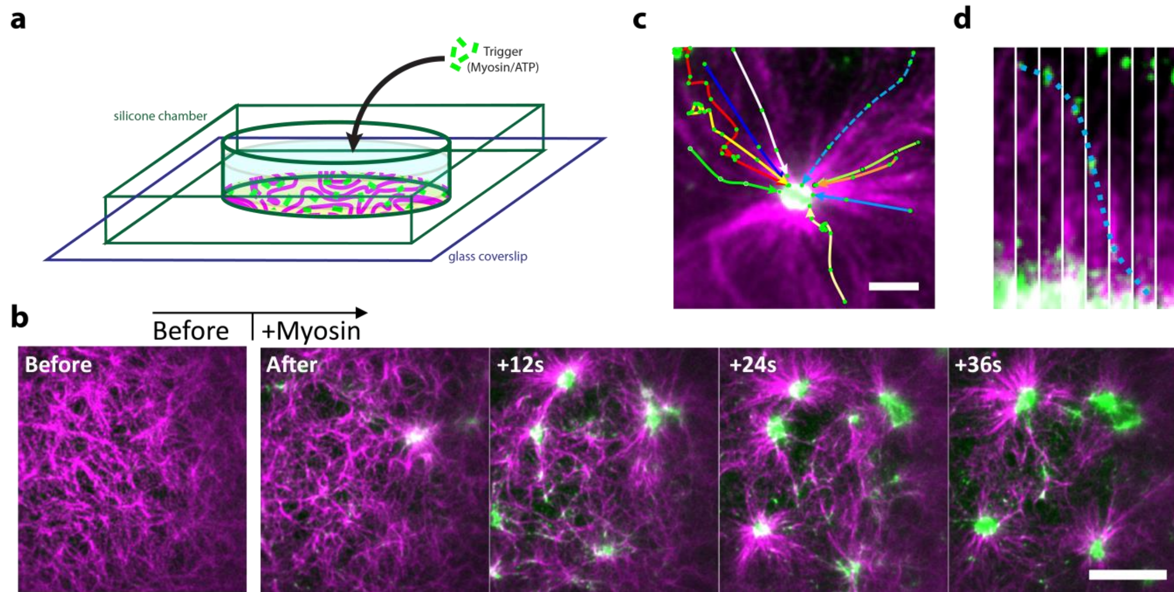

641

642 Fig. 1 | Myosin-induced actin network remodeling triggered by myosin addition. (a) An open chamber
643 allows myosin or ATP to be added while the network located near the glass bottom is observed by time-
644 lapse TIRF. (b) The initially disordered actin network (magenta) is rapidly remodeled by myosin (green)
645 into asters. Scale bar is 20 µm and seconds after myosin addition are noted in the upper-left corner of
646 the images. (c) Still image of an aster superposed with myosin trajectories (green data points connected
647 by lines) measured over 206 s. Myosins move to the center of the aster indicating that actin filaments
648 are polarity sorted with their plus ends oriented inwards. Scale bar is 5 µm. (d) Kymograph showing a
649 myosin filament moving to the center of the aster. The trajectory corresponds to the blue dashed arrow
650 in panel (c). Time between frames is 2 s.

651

bioRxiv preprint doi: https://doi.org/10.1101/314484; this version posted May 4, 2018. The copyright holder for this preprint (which was not certified by peer review) is the author/funder. All rights reserved. No reuse allowed without permission.

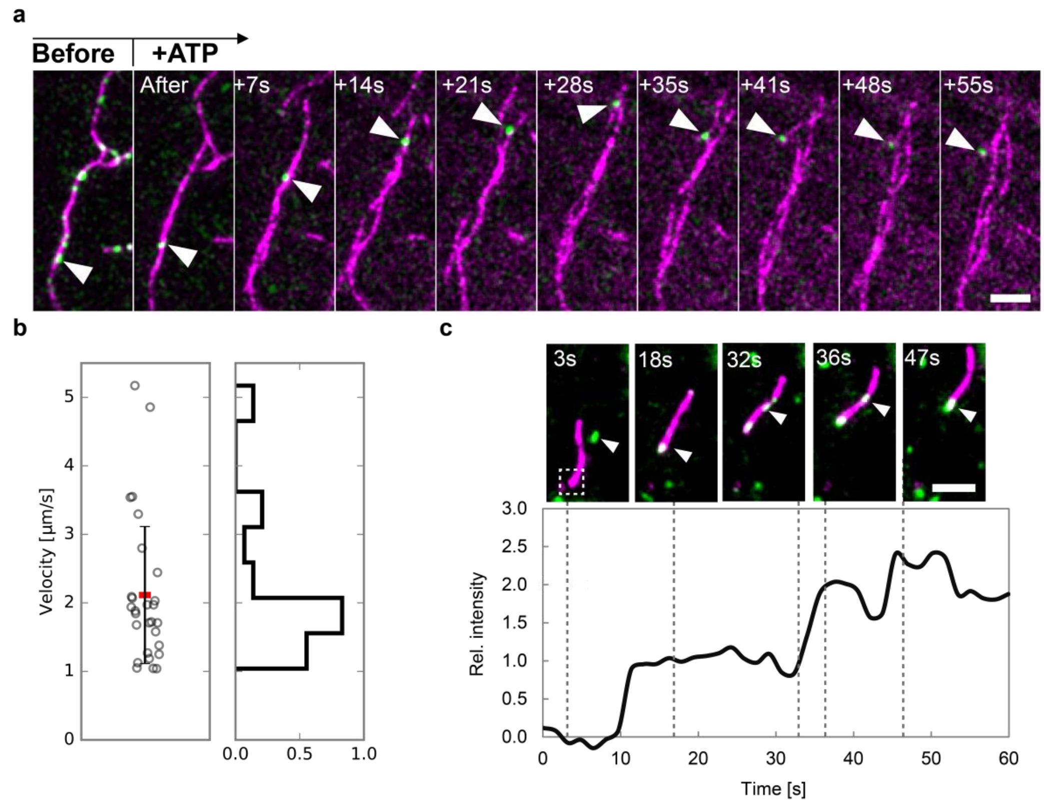

652

653

654 Fig. 2 | Myosin-actin interaction at low filament concentration. (a) Before ATP is added (left panel),
655 myosin binds to actin and is immobile. Upon addition of ATP, most myosin filaments detach; one
656 remaining filament runs along an actin filament, switches track as it encounters another actin filament at
657 28s, and runs on the new filament until it reaches the end and dwells there. Scale bar is 5 µm. (b) Left:
658 velocities of myosins running along actin. Every data point corresponds to one myosin trajectory (n = 28).
659 The horizontal red bar indicates the mean value (2 µm/s) and the error bar the standard deviation (1
660 µm/s). Right: Distribution of velocities. The velocity was only measured while myosin is moving.(b)
661 Myosin accumulation at actin filament ends. Top: Three myosin filaments bind to an actin filament and
662 move to the end. Bottom: Increase of fluorescence (Alexa Fluor 488) at the end of the actin filament
663 (measured in the region indicated by white box in first panel above). The intensity is normalized to the
664 intensity of the first myosin filament that reaches the actin end. Scale bar is 5 µm.

665

bioRxiv preprint doi: https://doi.org/10.1101/314484; this version posted May 4, 2018. The copyright holder for this preprint (which was not certified by peer review) is the author/funder. All rights reserved. No reuse allowed without permission.

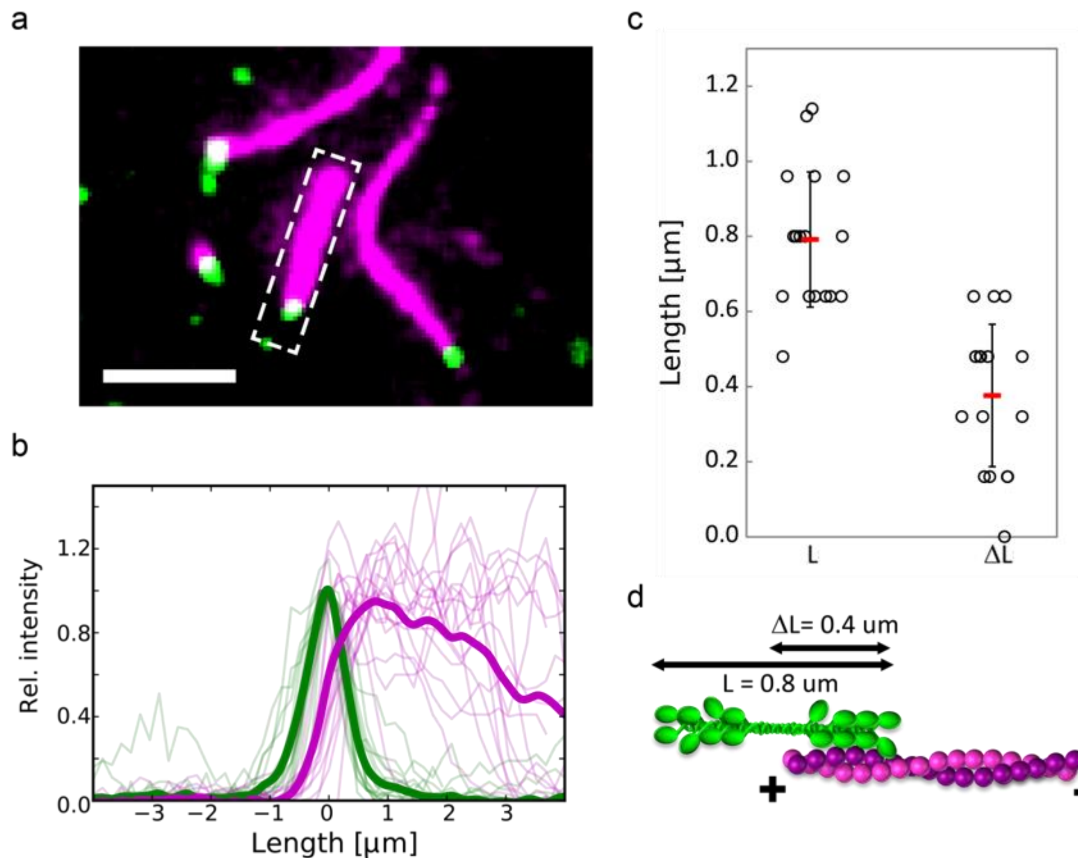

666

667

668 Fig. 3 | Position of myosin at actin filament ends. (a) Examples of myosin (green) dwelling on actin
669 (magenta) filament ends. Scale bar is 5 µm. (b) Intensity line profiles of actin and myosin for 17 events
670 (thin lines). Pairs of actin and myosin profiles are aligned with respect to the myosin peak intensity. The
671 intensities are normalized to the peak intensity for each profile. Thick lines show the average profiles. (c)
672 From the line profiles, we extract an average myosin filament length of 0.8 µm ± 0.2 µm (left) and an
673 average overlap between end-dwelling myosin and actin filaments of 0.4 µm ± 0.2 µm (right); red bars
674 indicate the mean values, error bars the standard deviation. (d) Schematic representation of myosin end-
675 dwelling. As myosin only overlaps by about half of its total length, we suggest that the trailing end is
676 involved in end-dwelling.

677

bioRxiv preprint doi: https://doi.org/10.1101/314484; this version posted May 4, 2018. The copyright holder for this preprint (which was not certified by peer review) is the author/funder. All rights reserved. No reuse allowed without permission.

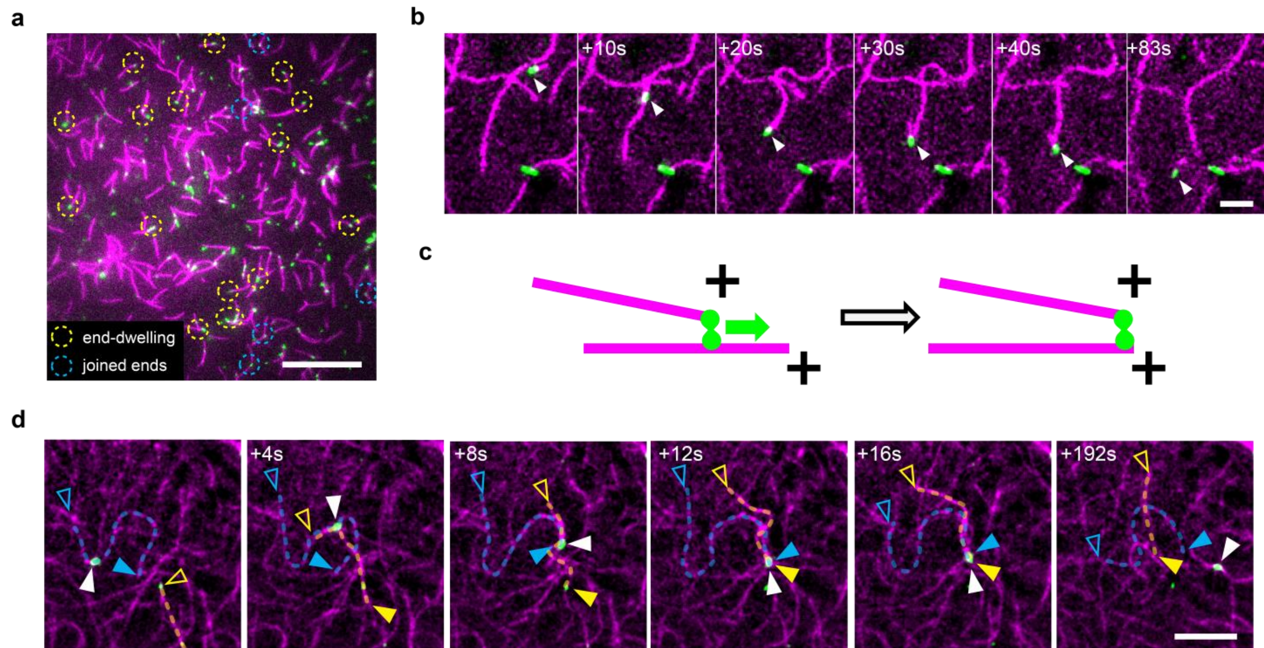

678

679

680 Fig. 4 | Myosin motility and end-dwelling as a mechanism for polarity sorting. (a) Myosin dwelling on
681 actin ends (yellow circles) or connecting two filaments by their ends (cyan circles) in in conditions
682 favoring sparse actin networks (see Table S1 for conditions). Scale bar is 20 µm. (b) Incipient asters
683 forming in networks with intermediate numbers of filaments actin filament. Myosin attached to a short
684 actin filament at t=0 encounters another actin filament at 10s and runs along it while staying attached to
685 the first one, keeping the two filament ends together until it detaches from one at 83 s. Scale bar is 5
686 µm. (c) Schematic representation of the process of myosin-driven polarity sorting. Dwelling on one
687 filament end, myosin transports the plus end as it runs along another filament and eventually joins the
688 two plus ends. (d) Aster formation in networks with higher numbers of filaments. Myosin (white arrow
689 head) runs along a filament (blue arrowheads and dashed line), encounters a second filament (yellow
690 arrow heads and dashed line), and moves along both filaments, joining their plus ends. This configuration
691 is stable for several tens of seconds. Scale bar is 10 µm, filled/empty arrow heads indicate plus/minus
692 ends.

693

bioRxiv preprint doi: https://doi.org/10.1101/314484; this version posted May 4, 2018. The copyright holder for this preprint (which was not certified by peer review) is the author/funder. All rights reserved. No reuse allowed without permission.

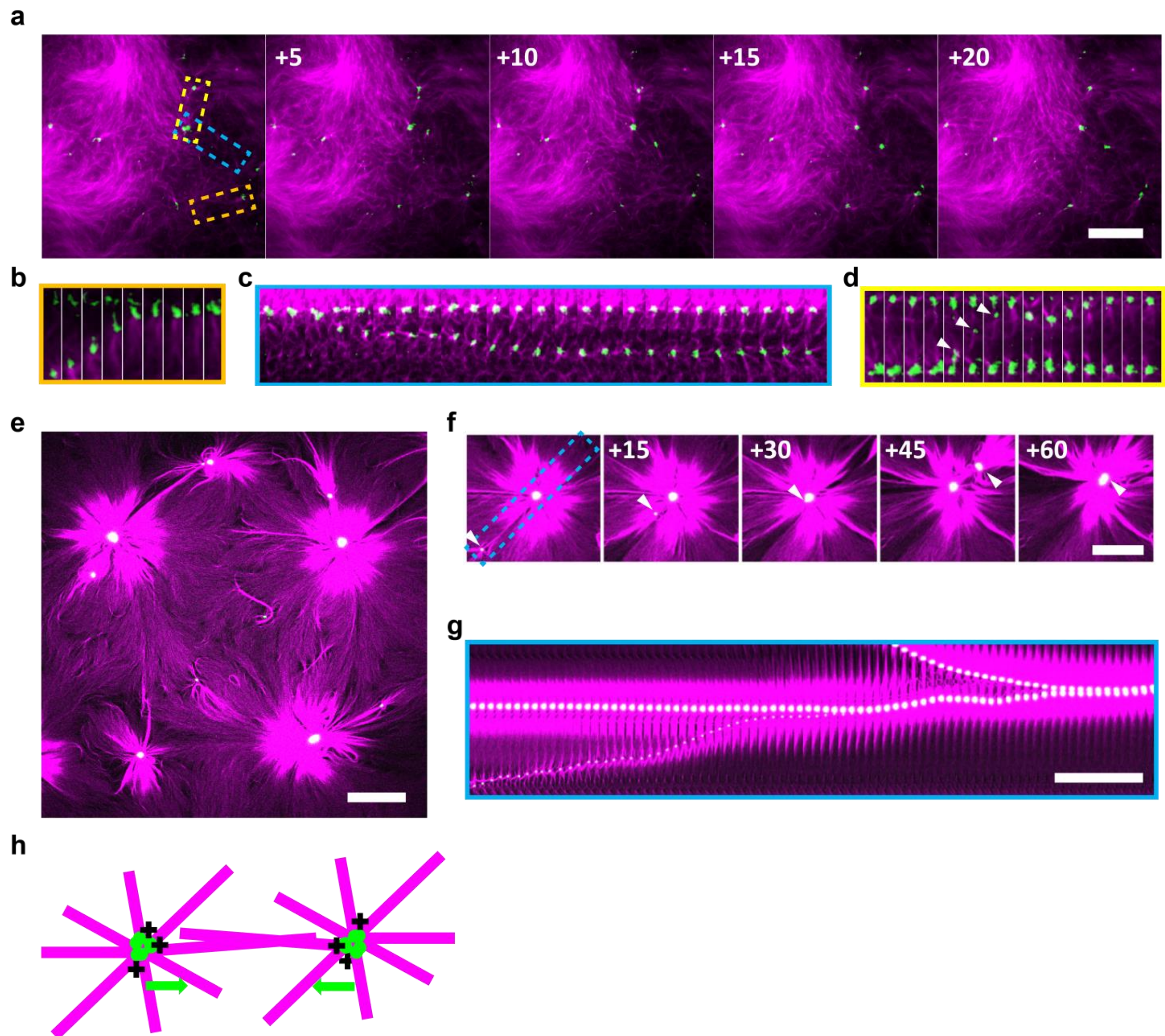

694

695

696 Fig. 5 | Effect of α-actinin-1 on myosin-mediated actin network remodeling. (a) In the absence of α-
697 actinin-1, myosin (green) forms small actin asters (magenta). Time in seconds, scale bar is 20 µm. (b, c, d)
698 Kymographs corresponding to the regions indicated by rectangles in panel (a) in corresponding colors.
699 Time between frames = 1 s. (b) Joining of two asters. (c) Aster splitting in two. (d) Exchange of myosin
700 between asters (arrow head). (e) In the presence of α-actinin (R_C = 0.01), myosin remodels actin into
701 large asters. Scale bar is 50 µm. (f) Two subsequent events where neighboring asters move towards each
702 other in a persistent manner and eventually join. Time in min, scale bar is 50 µm. (g) Kymograph along
703 the dashed line in (f). Scale bar is 10 min. (h) Schematic showing how neighboring asters move towards
704 each other due to their polar nature.

705

706

bioRxiv preprint doi: https://doi.org/10.1101/314484; this version posted May 4, 2018. The copyright holder for this preprint (which was not certified by peer review) is the author/funder. All rights reserved. No reuse allowed without permission.

707

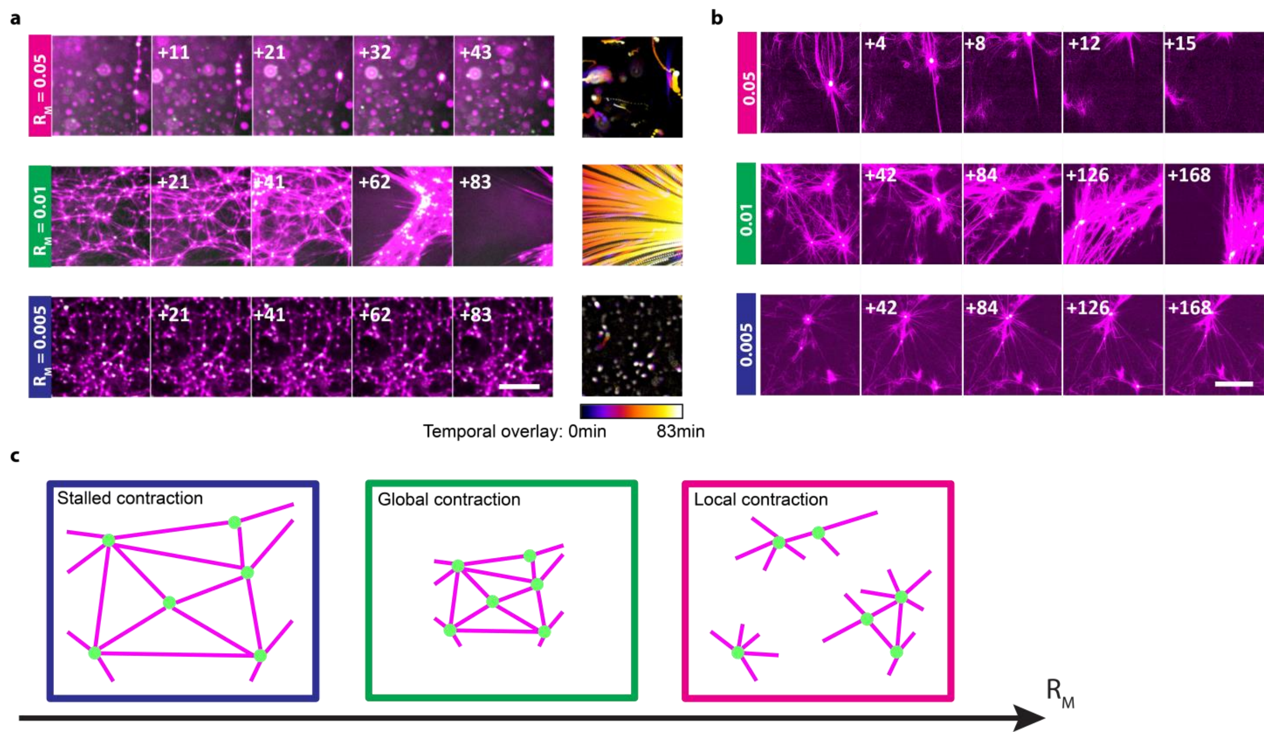

708

709 Fig. 6 | Asters formed at different motor:actin concentration ratios, R_M. (a) At R_M = 0.05, asters form and
710 locally contract the network. For R_M = 0.01, asters form and and become part of a percolating network
711 that exhibits global contraction. For R_M = 0.005, the network is stalled and does not contract, although
712 asters are still present. Time in min, scale bar 200 µm. (b) Higher magnification images show that asters
713 are formed in the three regimes. Time in min, scale bar 50 µm. (c) Schematic representation of the three
714 contraction regimes as a function of R_M.

715

bioRxiv preprint doi: https://doi.org/10.1101/314484; this version posted May 4, 2018. The copyright holder for this preprint (which was not certified by peer review) is the author/funder. All rights reserved. No reuse allowed without permission.

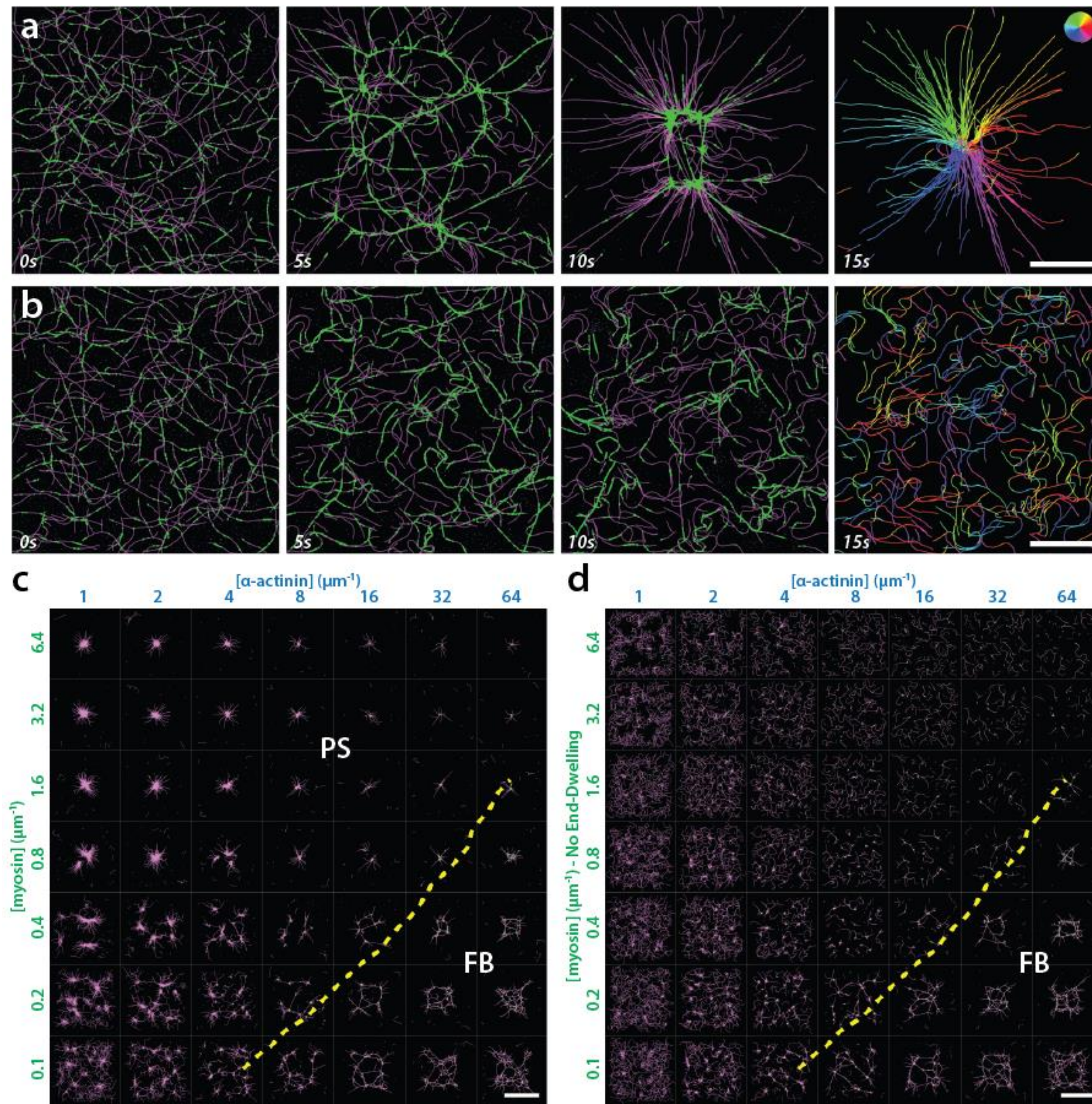

716

717 Fig. 7 | Role of end-dwelling in simulated networks with parameters corresponding to *in vitro*
718 experimental conditions. (a, b) Time series of simulations with 200 flexible filaments ("actin", in
719 magenta) with average lengths of 10 μm, and myosin minifilaments ("myosin", in green). Myosin motors
720 are plus-end directed and modeled (a) with or (b) without end-dwelling. The last time point shows actin
721 filaments segments colored according to their orientation. In (a) asters form with all filament plus ends
722 at the center of the aster as a result of the polarity sorting mechanism. Without end-dwelling (b), the
723 network does not contract. (a, b) Scale bar 10 μm. (c, d) Phase diagrams of simulated networks after
724 200s of simulation with varying concentrations of α-actinin and myosins (c) with or (d) without end-
725 dwelling motors. Concentrations of α-actinin and myosin are given as molecules per μm of actin
726 filament. Actin filament lengths as in (a, b) with mesh-size of 1.1 μm. In the region above the dashed
727 yellow line, contraction is dominated by Polarity Sorting (PS), as shown by the fact that contraction is lost
728 without myosing end-dwelling. In the region below, contraction persists also without myosin end-
729 dwelling, showing it is mediated by Filament Buckling (FB). (c, d) Scale bar 40 μm.

bioRxiv preprint doi: https://doi.org/10.1101/314484; this version posted May 4, 2018. The copyright holder for this preprint (which was not certified by peer review) is the author/funder. All rights reserved. No reuse allowed without permission.

730

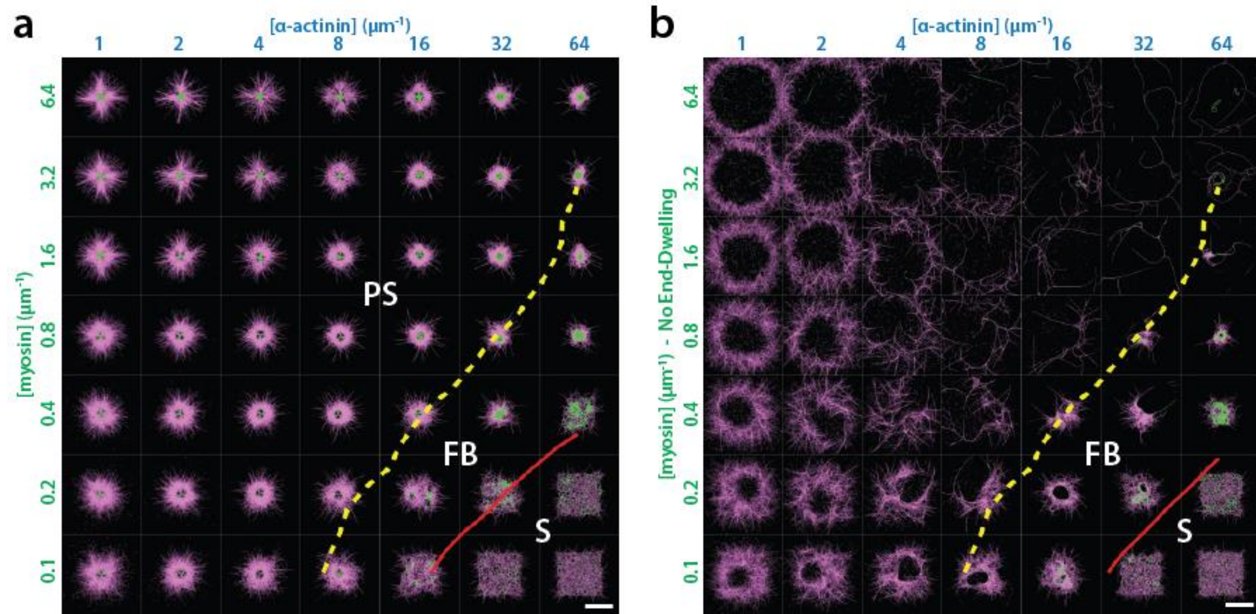

731

732 Fig. 8 | Role of end-dwelling in simulated networks with parameters corresponding to the actin
733 cortex *in vivo*. (a, b) Phase diagrams of simulated networks after 80s of simulation with average actin
734 filaments lengths of 1 μm, mesh-size of 0.1 μm and varying concentrations of α-actinin and myosins
735 (a) with and (b) without end-dwelling motors. Concentrations of α-actinin and myosin are given as
736 molecules per μm of actin filament. Dashed yellow lines demarcate the regions where contraction is
737 dominated by Polarity Sorting (PS) or Filament Buckling (FB), as described in Fig. 7. Solid red lines
738 indicate the boundaries between contractile and Stalled (S) regions in each phase diagram. Scale bar
739 4 μm.